Supplemental Information

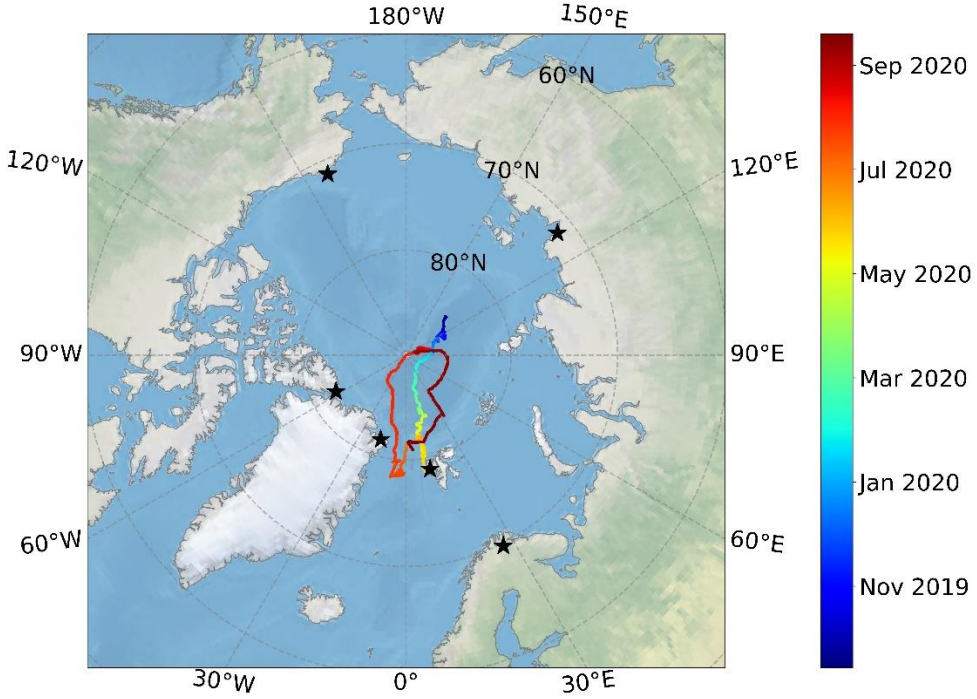

Figure S1. The location of *Polarstern* during the MOSAiC expedition. The color bar shows the time of year. Adapted from Boyer et al. (2023).

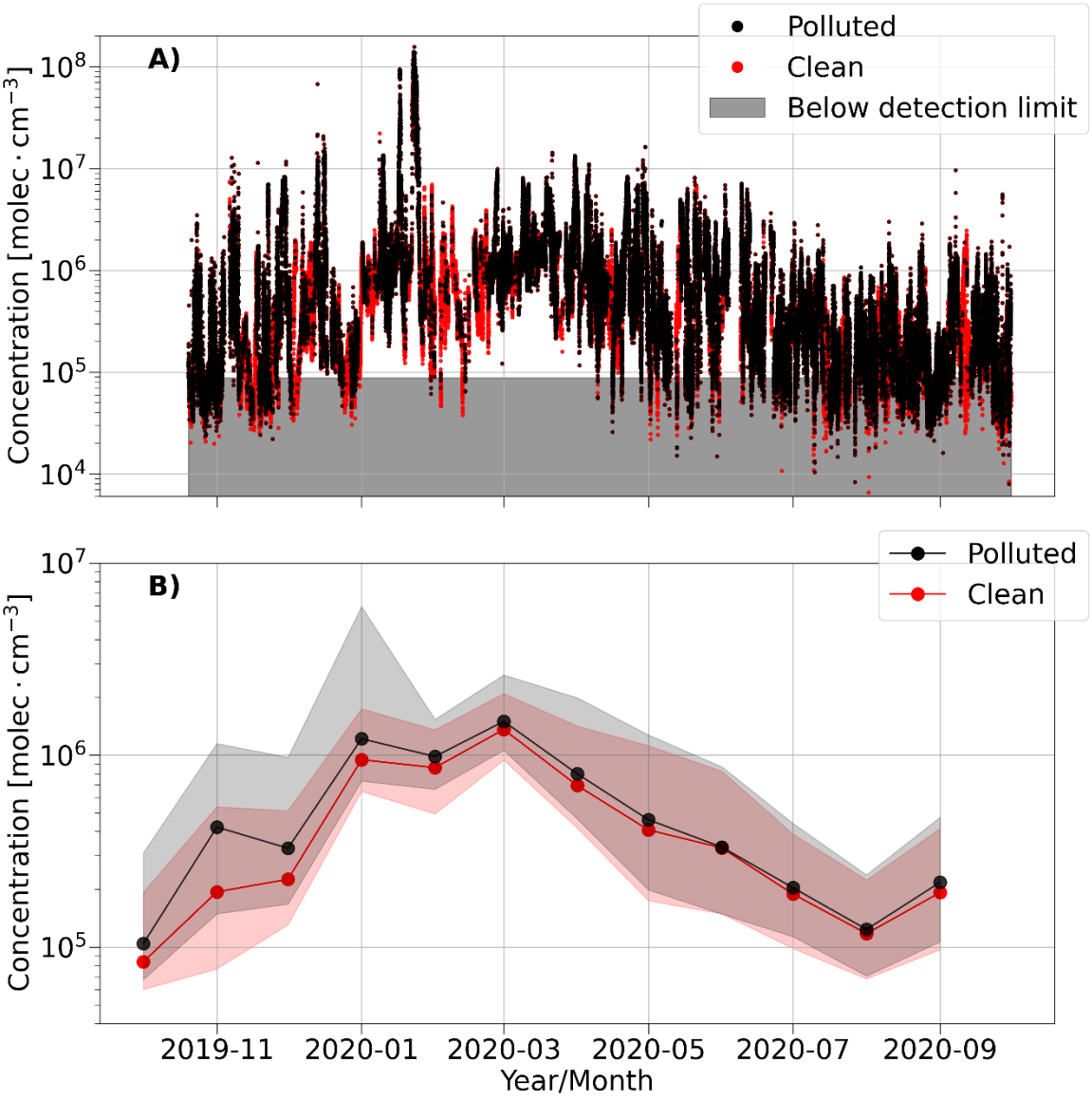

Figure S2. Comparison of sulfuric acid concentrations during clean and polluted periods. A) The timeseries of SA concentration at 5-minute resolution color coded according to polluted (black) and clean (red) periods. The polluted periods are influenced by local pollution from the ship stack, as identified by a pollution detection algorithm (Beck et al., 2022) applied to particle concentrations from a condensation particle counter (TSI, model 3025) that was collocated with the NO_3-CIMS in the *Swiss* container. The dark gray shaded region shows the concentrations that are below the determined SA detection limit. B) The monthly median concentrations for polluted (black) and clean (red) periods. The shaded regions show the interquartile range for each respective period. Note that the interquartile ranges in this figure also include the concentrations below the detection limit.

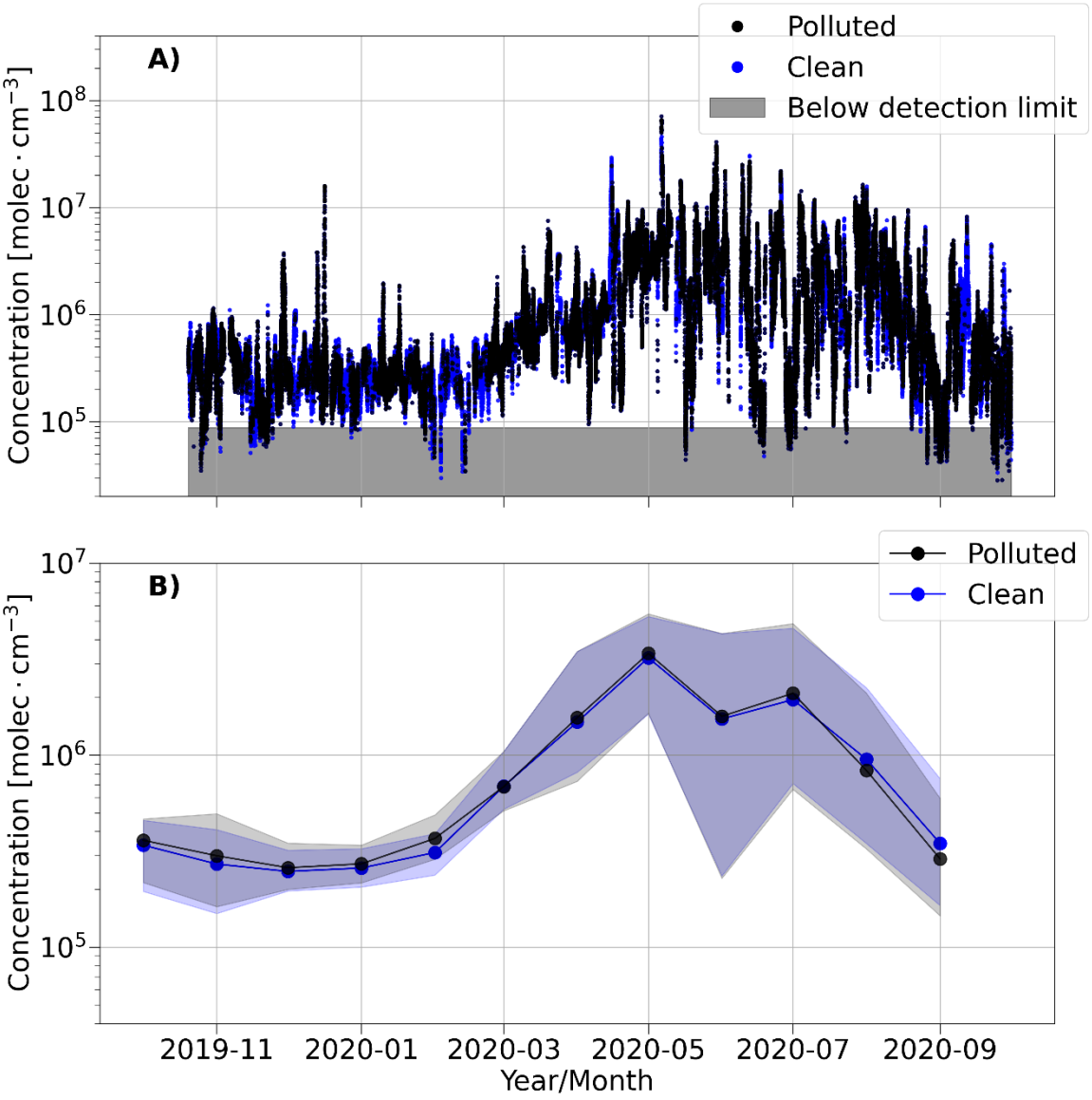

Figure S3. Comparison of methanesulfonic acid concentrations during clean and polluted periods. A) The timeseries of MSA concentration at 5-minute resolution color coded according to polluted (black) and clean (blue) periods. The polluted periods are influenced by local pollution from the ship stack, as identified by a pollution detection algorithm (Beck et al., 2022) applied to particle concentrations from a condensation particle counter (TSI, model 3025) that was collocated with the NO_3-CIMS in the *Swiss* container. The dark gray shaded region shows the concentrations that are below the determined MSA detection limit. B) The monthly median concentrations for polluted (black) and clean (blue) periods. The shaded regions show the interquartile range for each respective period. Note that the interquartile ranges in this figure also include the concentrations below the detection limit.

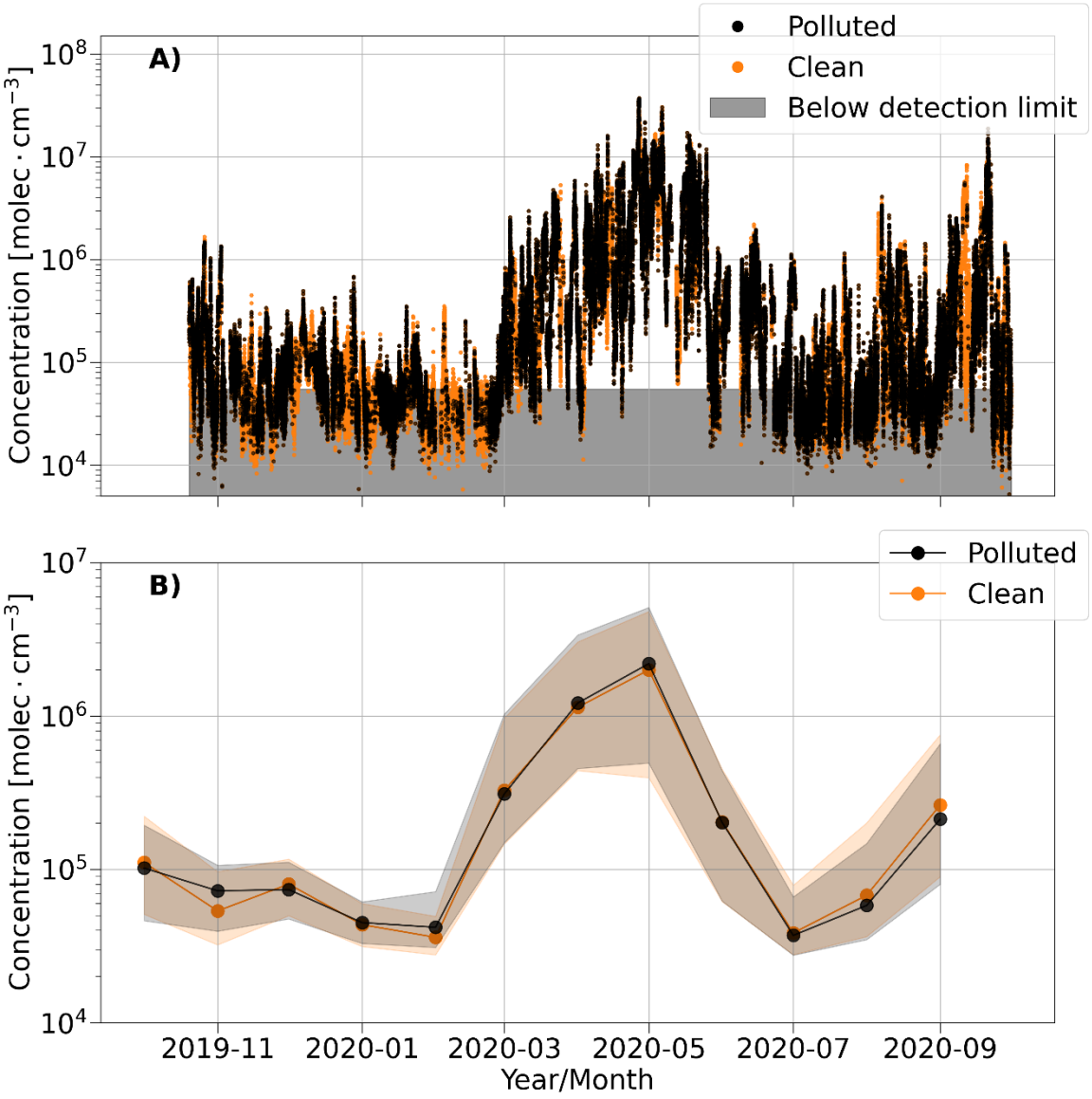

Figure S4. Comparison of iodic acid concentrations during clean and polluted periods. A) The timeseries of IA concentration at 5-minute resolution color coded according to polluted (black) and clean (orange) periods. The polluted periods are influenced by local pollution from the ship stack, as identified by a pollution detection algorithm (Beck et al., 2022) applied to particle concentrations from a condensation particle counter (TSI, model 3025) that was collocated with the NO_3-CIMS in the *Swiss* container. The dark gray shaded region shows the concentrations that are below the determined IA detection limit. B) The monthly median concentrations for polluted (black) and clean (red) periods. The shaded regions show the interquartile range for each respective period. Note that the interquartile ranges in this figure also include the concentrations below the detection limit.

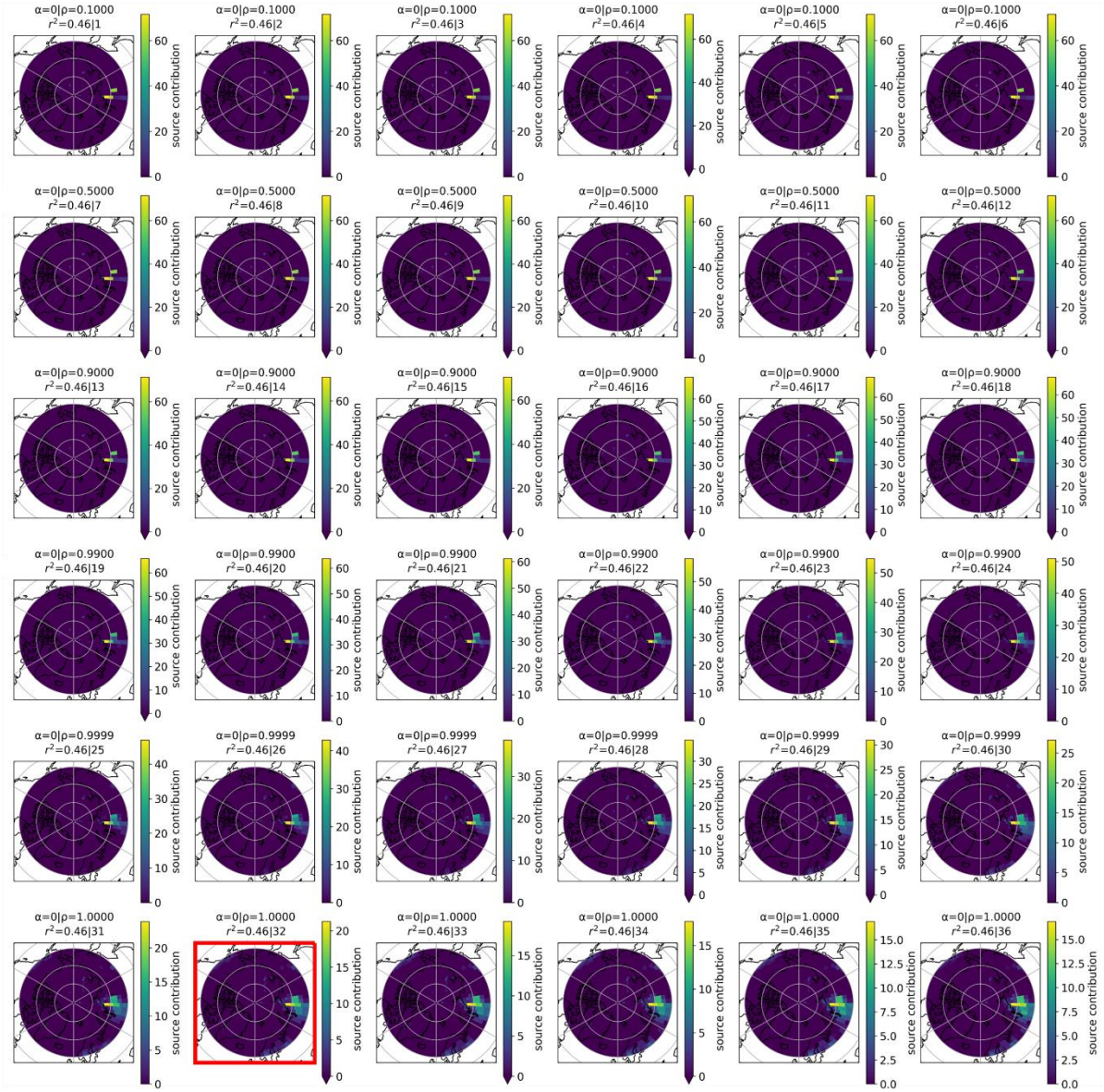

Figure S5. The 36 source region footprint maps of SO_2 produced using the iterative elastic net regularization method in the inverse model. The polygons represent the source region locations identified by the inverse model for various levels of penalization in the elastic net regression method. The elastic net regularization parameters α and ρ, as described in Section 2.6, are included above each map, as well as the correlation coefficient (r^2) and the iteration number. Iteration 32, outlined in red, was selected in this analysis as it represents known source regions while minimizing noisy regions.

Figure S6. The 36 source region footprint maps of SA produced using the iterative elastic net regularization method in the inverse model. The polygons represent the source region locations identified by the inverse model for various levels of penalization in the elastic net regression method. The elastic net regularization parameters α and ρ, as described in Section 2.6, are included above each map, as well as the correlation coefficient (r^2) and the iteration number. The Iteration 24, outlined in red, was selected in this analysis as it represents known source regions while minimizing noisy regions.

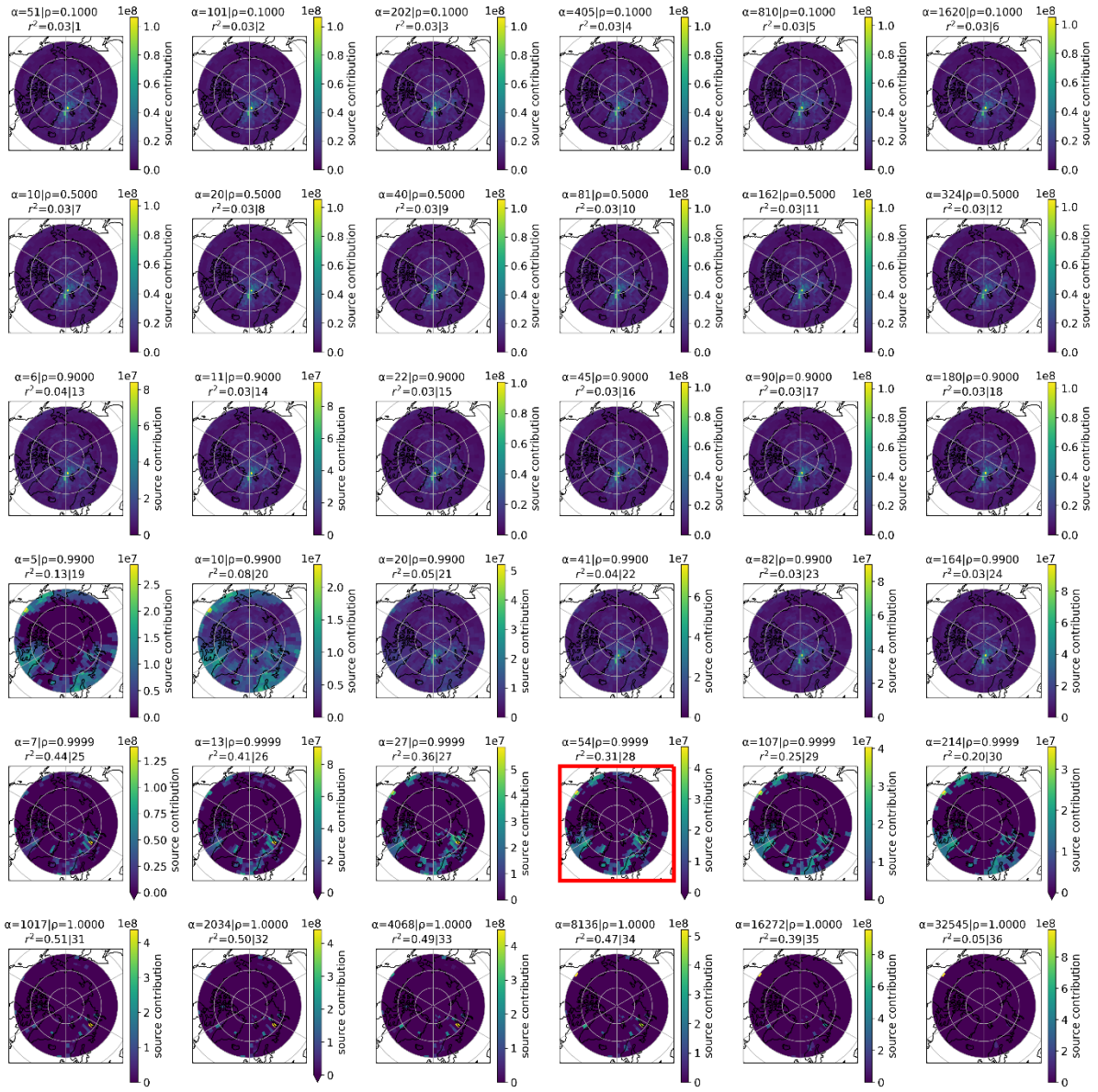

Figure S7. The 36 source region footprint maps of MSA produced using the iterative elastic net regularization method in the inverse model. The polygons represent the source region locations identified by the inverse model for various levels of penalization in the elastic net regression method. The elastic net regularization parameters α and ρ, as described in Section 2.6, are included above each map, as well as the correlation coefficient (r^2) and the iteration number. Iteration 28, outlined in red, was selected in this analysis as it represents known source regions while minimizing noisy regions.

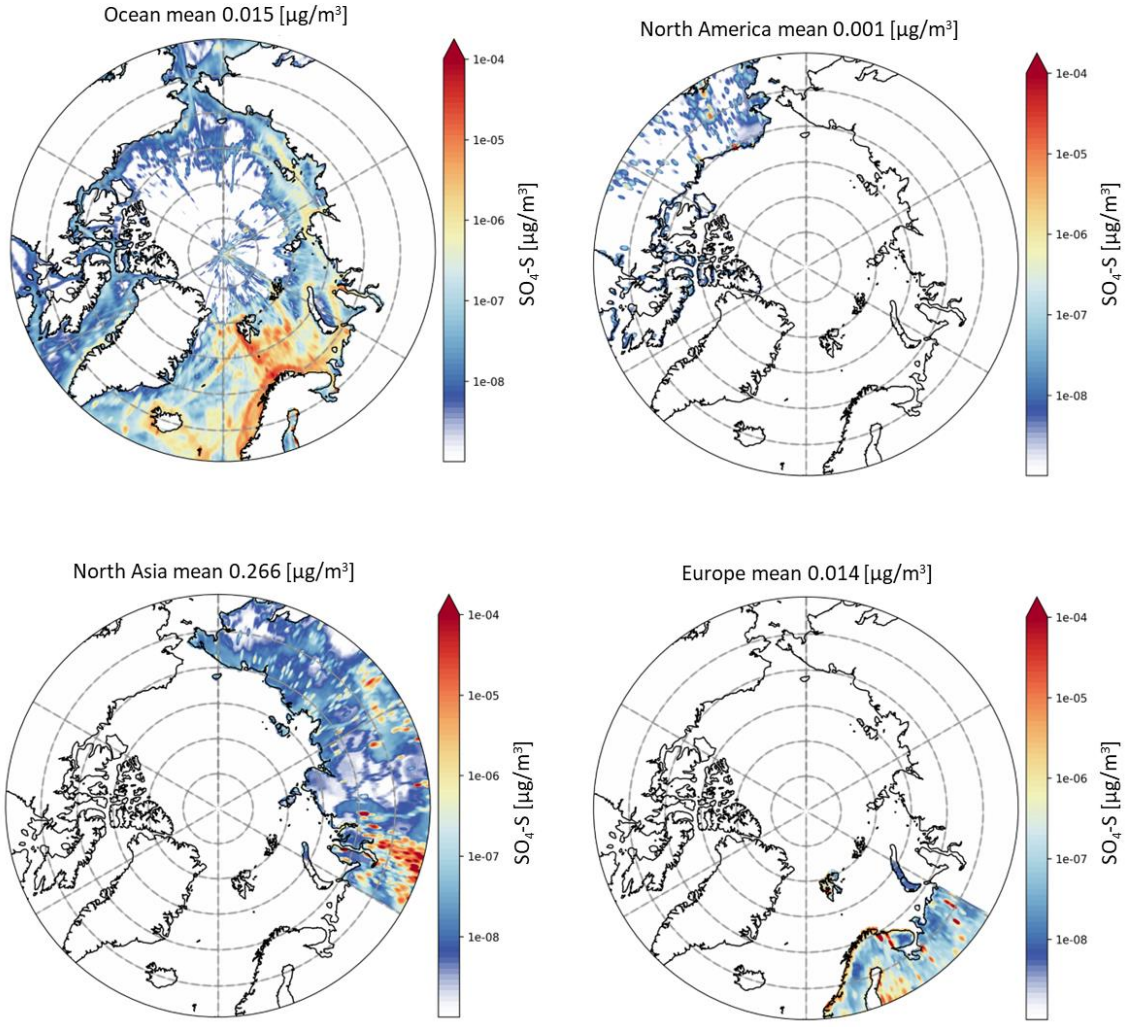

Figure S8. Annual average source contribution maps of SO_4-S by source region from the ECLIPSE v6b emission inventory. The SO_4-S concentrations, or anthropogenic particulate sulfate mass derived from SO_2 emissions, are presented as the yearly averages according to different geographic source regions.

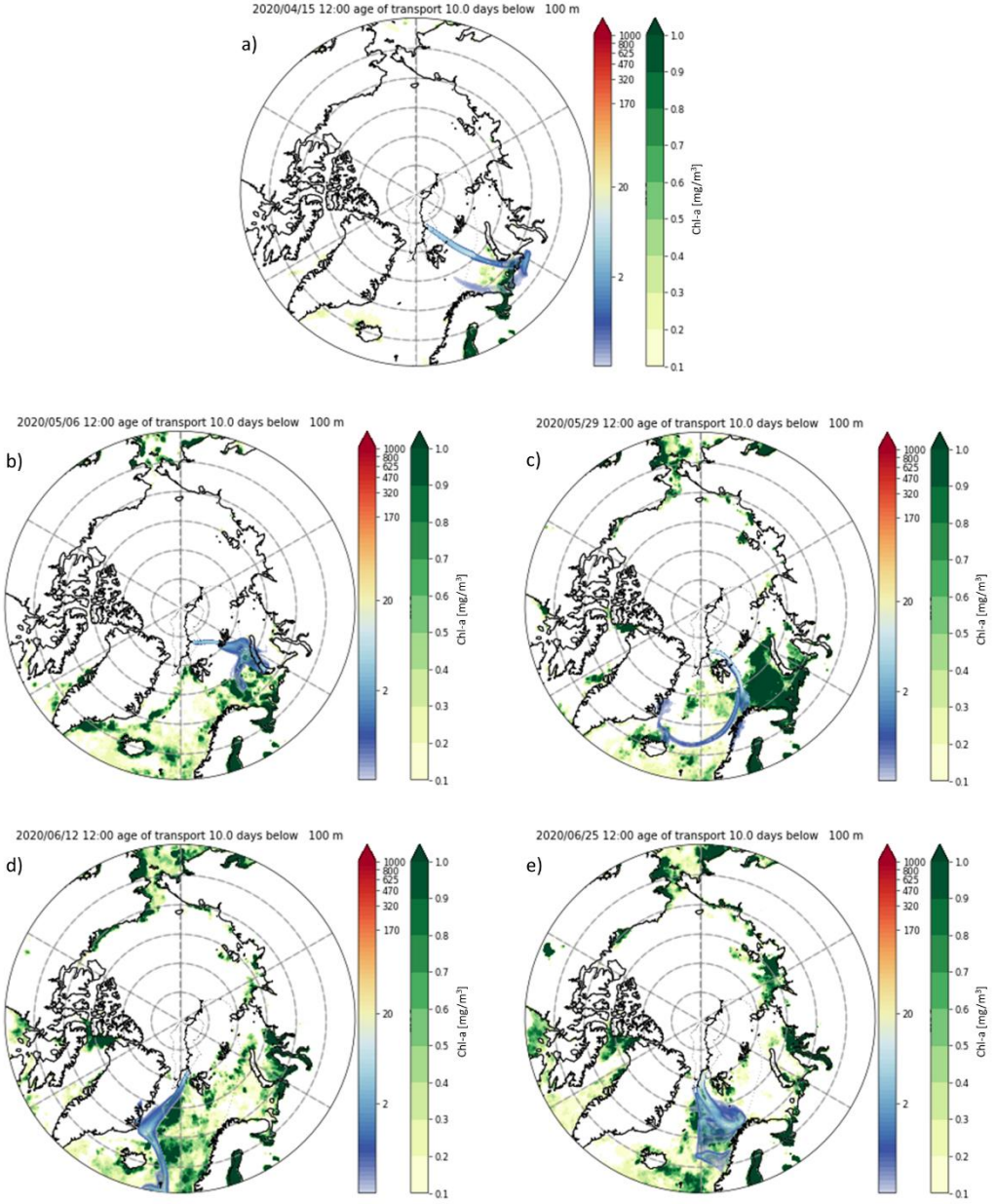

Figure S9. FLEXPART trajectories coupled with chl-a concentrations. Maps of individual, 10-day air mass trajectories in the lower 100 m altitude for a) April 15, 2020; b) May 06, 2020; c) May 29, 2020; d) June 12, 2020; and e) June 25, 2020 are shown with the chl-a concentrations (green colorbar) from the OC-CCI dataset. The air tracer is indicated by the blue-red colorbar.

References

Beck, I., Angot, H., Baccarini, A., Dada, L., Quéléver, L., Jokinen, T., Laurila, T., Lampimäki, M., Bukowiecki, N., Boyer, M., Gong, X., Gysel-Beer, M., Petäjä, T., Wang, J., and Schmale, J.: Automated identification of local contamination in remote atmospheric composition time series, Atmospheric Meas. Tech., 15, 4195–4224, https://doi.org/10.5194/amt-15-4195-2022, 2022.

Boyer, M., Aliaga, D., Pernov, J. B., Angot, H., Quéléver, L. L. J., Dada, L., Heutte, B., Dall'Osto, M., Beddows, D. C. S., Brasseur, Z., Beck, I., Bucci, S., Duetsch, M., Stohl, A., Laurila, T., Asmi, E., Massling, A., Thomas, D. C., Nøjgaard, J. K., Chan, T., Sharma, S., Tunved, P., Krejci, R., Hansson, H. C., Bianchi, F., Lehtipalo, K., Wiedensohler, A., Weinhold, K., Kulmala, M., Petäjä, T., Sipilä, M., Schmale, J., and Jokinen, T.: A full year of aerosol size distribution data from the central Arctic under an extreme positive Arctic Oscillation: insights from the Multidisciplinary drifting Observatory for the Study of Arctic Climate (MOSAiC) expedition, Atmospheric Chem. Phys., 23, 389–415, https://doi.org/10.5194/acp-23-389-2023, 2023.